Published in final edited form as:
Int j numer method biomed eng. 2013 November ; 29(11): 1192–1213. doi:10.1002/cnm.2568.

Validation of an open source framework for the simulation of blood flow in rigid and deformable vessels

T. Passerini[1], **A. Quaini**[2,*], **U. Villa**[1], **A. Veneziani**[1], and **S. Canic**[2]

[1]Department of Mathematics and Computer Science, Emory University, 400 Dowman Drive, Atlanta GA 30322, USA

[2]Department of Mathematics, University of Houston, 4800 Calhoun Rd., Houston TX 77204, USA

SUMMARY

We discuss in this paper the validation of an open source framework for the solution of problems arising in hemodynamics. The proposed framework is assessed through experimental data for fluid flow in an idealized medical device with rigid boundaries and a numerical benchmark for flow in compliant vessels. The core of the framework is an open source parallel finite element library that features several algorithms to solve both fluid and fluid-structure interaction problems. The numerical results for the flow in the idealized medical device (consisting of a conical convergent, a narrow throat, and a sudden expansion) are in good quantitative agreement with the measured axial components of the velocity and pressures for three different flow rates corresponding to laminar, transitional, and turbulent regimes. We emphasize the crucial role played by the accuracy in performing numerical integration, mesh, and time step to match the measurements. The numerical fluid-structure interaction benchmark deals with the propagation of a pressure wave in a fluid-filled elastic tube. The computed pressure wave speed and frequency of oscillations, and the axial velocity of the fluid on the tube axis are close to the values predicted by the analytical solution associated with the benchmark. A detailed account of the methods used for both benchmarks is provided.

Keywords

Computational fluid dynamics; hemodynamics; experimental validation; fluid-structure interaction

1. INTRODUCTION

Computational fluid dynamics (CFD) is nowadays a tool of choice for the investigation of blood flow problems. It has been extensively applied over the years to study the physiology and physiopathology of the cardiovascular system [1, 2, 3] and to patient-specific planning of interventions for cardiovascular disease [4, 5, 6]. It has been used in the medical device industry to develop and/or analyze the performance of prosthetic heart valves [7], stents [8, 9], ventricular assist devices [10], blood filters [11] etc. In addition, CFD results are also being used by some manufacturers to help demonstrate safety and efficacy of a device as part of the pre-market device submissions to the U.S. Food and Drug Administration (FDA) [12].

However, the reliability of the computational approach to the study of physics phenomena is dependent on the *validation* of the mathematical models and the *verification* of the

*Correspondence to: A. Quaini, Department of Mathematics, University of Houston, Houston TX 77204, USA. quaini@math.uh.edu.

numerical methods [13]. A verified method is capable of correctly solving the problem equations, while a valid model is able to correctly describe the features of the problem (i.e., it uses the right equations).

In 2004, the FDA launched a “Critical Path Initiative” program [14] aimed, among other things, at improving the use and validating CFD techniques in the evaluation of medical devices. A benchmark nozzle model was developed which contains all the features commonly encountered in medical devices (flow contraction and expansion, recirculation zones etc., see Figure 1) and three laboratories were asked to perform flow visualization experiments on fabricated models for five flow rates spanning laminar, transitional, and turbulent regimes [12]. This resulted in benchmark data available online to the scientific community for the validation of CFD simulations [15]. Other significant efforts towards the definition of a shared test bed for numerical solvers for partial differential equations, and specifically for flow problems, include the works by Turek and coworkers for the verification of solvers for the Navier-Stokes equations [16] and for the fluid-structure interaction problem [17, 18].

The results of a first CFD study of the FDA nozzle model are reported in [19]. Twenty-eight groups of CFD professionals around the world participated in the study, following different modeling approaches (turbulence models vs. direct numerical simulations, 2D vs. 3D geometries, choice of the boundary conditions etc). Overall, the results obtained by different groups had a very large variability, also with respect to the experimental results. It was observed that turbulence models were in general unable to correctly estimate the centerline velocities in the inlet and throat of the nozzle, and velocities and shear stresses in the recirculation zones downstream of the sudden expansion. Limitations of direct numerical simulations when dealing with flows in the transitional regime were also discussed, most likely due to under-resolution of the computational grid. One of the conclusions of the study was the recommendation that validation studies should always be performed when attempting the use of computational models for the evaluation of medical devices.

Our goal is two-fold: (i) validate an open source CFD framework for the solution of problems of interest in hemodynamics and (ii) provide a detailed report on the methodology that we use, to make our experiences reproducible. To achieve this goal we refer to (a) the FDA benchmark; (b) the FSI test case presented in [20]. The former is intended to assess the code capabilities in simulating fluid flow in a rigid domain representative of a medical device. The latter is intended to evaluate the performance of the software in simulating fluid flow in deformable domains, which is clearly of utmost relevance for cardiovascular problems. In particular - in absence of an analogue of the FDA benchmark including FSI - the second test deals with the propagation of a pressure wave in a fluid-filled elastic cylindrical vessel for which an analytical solution for the wave speed and frequency of oscillation are provided.

The core of our open-source CFD framework is LifeV [21], an open source library of algorithms and data structures for the numerical solution of partial differential equations with high performance computing (HPC) technologies. High performance computing is supported by LifeV through the interplay with third-party software (in particular the linear algebra package Trilinos [22] by Sandia National Laboratories). LifeV is maintained and developed by an international network of universities and research centers across Europe and the US, whose core members are the Politecnico di Milano (Italy), the École Polytechnique Fédérale de Lausanne (Switzerland), and Emory University in Atlanta (USA). Other institutions contribute to the project, including the INRIA in Paris (France), Florida State University, Georgia Institute of Technology, and the University of Houston.

LifeV has been used over the last ten years as a valuable tool for the prototyping of numerical methods (see e.g. [23, 24, 25, 26, 27, 28]). Moreover, software based on LifeV has been extensively used in research projects focused on the modeling of blood flow problems, among others the drug release from implantable stents [29], the design of medical procedures in cardiology [30], the optimization of diagnostic procedures [31], surgical planning [32] and the study of cerebral hemodynamics [33].

As part of the framework we also consider open source mesh generators, such as Netgen [34] and Gmsh [35], and software for visualization and post processing such as ParaView [36]. Both Netgen and Gmsh provide several algorithms for 3D mesh generation and mesh refinement. Their scripting languages allow to have a fine control on the features of the mesh when dealing with simple geometries (in particular axisymmetric domains). ParaView is a large software project based on VTK. In this context, it is recalled for its powerful graphical interface and for offering several filters to operate on the data from numerical simulation (to visualize, probe, process, …).

We discuss in this paper some of the the strengths of this framework, such as its open source nature, its solid mathematical background, its flexibility in handling complex geometries, and its performance on HPC machines. This work in fact represents a first step towards making such CFD framework a reliable tool for flow simulations in medical devices or biomechanics problems. Nonetheless, we also draw some conclusions (e.g., on which methods and algorithms work best in the different flow regimes) that are not restricted to this specific CFD framework, but rather are general and could be used as guidelines for similar CFD studies with different software.

The outline of the paper is as follows. In Section 2 we state the problems that we want to solve (fluid, structure, and coupled fluid-structure interaction problems). For each problem we touch on the numerical methods that we use for their discretization in time and space and discuss the solution of the associated linear systems. In Section 3, we describe the FDA benchmark and the numerical benchmark for FSI problems and we report the results of the validation and verification. Conclusions are drawn in Section 4.

2. PROBLEM DEFINITION

2.1. The fluid equations

The motion of an incompressible viscous fluid in a spatial domain (denoted hereafter by Ω_f) over a time interval of interest (t_0, T) is described by the Navier-Stokes equations

$$\rho_f \left(\frac{\partial \boldsymbol{u}}{\partial t} + (\boldsymbol{u} \cdot \nabla)\boldsymbol{u} \right) - \nabla \cdot \boldsymbol{\sigma}_f = \boldsymbol{g}_f \quad \text{in } \Omega_f \times (t_0, T), \quad (1)$$

$$\nabla \cdot \boldsymbol{u} = 0 \quad \text{in } \Omega_f \times (t_0, T), \quad (2)$$

where ρ_f is the fluid density, $\boldsymbol{u}$ is the fluid velocity, $\boldsymbol{\sigma}_f$ the Cauchy stress tensor and $\boldsymbol{g}_f$ the body force. For Newtonian fluids $\boldsymbol{\sigma}_f$ has the following expression

$$\boldsymbol{\sigma}_f(\boldsymbol{u}, p) = -p\mathbf{I} + 2\mu_f \boldsymbol{\varepsilon}(\boldsymbol{u}),$$

where p is the pressure, μ_f is the fluid dynamic viscosity, and $\boldsymbol{\varepsilon}(\boldsymbol{u}) = (\nabla \boldsymbol{u} + (\nabla \boldsymbol{u})^T)/2$ is the strain rate tensor. Equations (1)–(2) need to be supplemented with initial and boundary conditions.

In the following we focus on the problem of the flow of blood in a vessel (either rigid or deformable). For such a problem, it is commonly accepted to ignore any body force (including the gravity force).

The Reynolds number can be used to characterize the flow regime, and identify the transition of the flow to turbulence. We define the Reynolds number as

$$Re = \frac{\overline{u} D}{\nu_f} \quad (3)$$

where $\bar{u}$ is the mean sectional velocity within a pipe of hydraulic diameter D and $\nu_f = \mu_f/\rho_f$ is the fluid kynematic viscosity. The Reynolds number can be thought of as the ratio of inertial forces to viscous forces. For large Reynolds numbers, inertial forces are dominant over viscous forces and *vice versa*.

2.1.1. Discretization—We approximate in time equations (1)–(2) by the backward differentiation formula of order 2 (BDF2 [37]) and we linearize the convective term by an extrapolation formula of the same order. Given $\Delta t \in \mathbb{R}$, let us set $t^n = t_0 + n\Delta t$, with $n = 0, \ldots, N_T$ and $T = t_0 + N_T \Delta t$. Problem (1)–(2) discretized in time reads: given $\boldsymbol{u}^n$, for $n \geq 1$, find the solution $(\boldsymbol{u}^{n+1}, p^{n+1})$ of the system:

$$\rho_f \frac{3\boldsymbol{u}^{n+1} - 4\boldsymbol{u}^n + \boldsymbol{u}^{n-1}}{2\Delta t} + \rho_f (2\boldsymbol{u}^n - \boldsymbol{u}^{n-1}) \cdot \nabla \boldsymbol{u}^{n+1} - \nabla \cdot \boldsymbol{\sigma}_f (\boldsymbol{u}^{n+1}, p^{n+1}) = \boldsymbol{0} \quad \text{in } \Omega_f, \quad (4)$$

$$\nabla \cdot \boldsymbol{u}^{n+1} = 0 \quad \text{in } \Omega_f. \quad (5)$$

For the space discretization, we introduce a conformal and quasi-uniform partition $\mathcal{T}_h^f$ of Ω_f made up of a certain number of tetrahedra. We will use two inf-sup stable finite element pairs: the $\mathbb{P}_1^b - \mathbb{P}_1$ elements and the $\mathbb{P}_2$-$\mathbb{P}_1$ elements and we will point out the strengths and limitations of both. For more details concerning the discretization of the Navier-Stokes problem, we refer, e.g., to [38]. We do not use any stabilization for the convective term: careful selection of the discretization parameters - time step and mesh size - yields stable solutions without the need for numerical stabilization techniques. Moreover, even though the semi-implicit treatment of the convective term in eq. (4) does not guarantee the unconditional stability in time of the numerical scheme, we encounter no stability issues in the numerical experiments described in Sec. 3.1 and 3.2.

Let us denote by M the mass matrix, K the diffusion matrix, N the matrix associated with the discretization of the convective term, and B the matrix associated with the discretization of the operator $(-\nabla \cdot)$. The linearization and full discretization of problem (1)–(2) yields the following system

$$\rho_f \frac{3}{2\Delta t} M \mathbf{u}^{n+1} + \mu_f K \mathbf{u}^{n+1} + \rho_f N \mathbf{u}^{n+1} + B^T \mathbf{p}^{n+1} = \mathbf{b}_u^{n+1}, \quad (6)$$

$$B\mathbf{u}^{n+1}=\mathbf{0}, \quad (7)$$

where $\mathbf{u}^{n+1}$ and $\mathbf{p}^{n+1}$ are the arrays of nodal values for velocity and pressure. The array $\mathbf{b}_u^{n+1}$ accounts for the contributions of solution at the previous time steps and the contribution that the boundary nodes give to the internal nodes.

Set $C=\rho_f \frac{3}{2\Delta t} M+\mu_f K+\rho_f N$. We can rewrite (6)–(7) in the form

$$A\mathbf{x}^{n+1}=\mathbf{b}_f^{n+1}, \quad (8)$$

where

$$A=\begin{bmatrix} C & B^T \\ B & 0 \end{bmatrix}, \quad \mathbf{x}^{n+1}=\begin{bmatrix} \mathbf{u}^{n+1} \\ \mathbf{p}^{n+1} \end{bmatrix}, \quad \mathbf{b}_f^{n+1}=\begin{bmatrix} \mathbf{b}_u^{n+1} \\ \mathbf{0} \end{bmatrix}. \quad (9)$$

At every time level t^{n+1}, to solve system (8) we use the left preconditioned GMRES method. As preconditioner, we use an upper-triangular variant of the pressure corrected Yosida splitting [23, 39] given by

$$P=\begin{bmatrix} C & B^T \\ 0 & S(S+BH(\mu_f K+\rho_f N)HB^T)^{-1}S \end{bmatrix}, \quad H=\frac{2\Delta t}{3\rho_f}M^{-1}, \quad S=-BHB^T. \quad (10)$$

The above preconditioner is a suitable approximation of the *U* factor in the exact block *LU* factorization of matrix *A* in (9):

$$A=LU, \quad L=\begin{bmatrix} I & 0 \\ BC^{-1} & I \end{bmatrix}, \quad U=\begin{bmatrix} C & B^T \\ 0 & -BC^{-1}B^T \end{bmatrix}. \quad (11)$$

See also [40, 41, 42, 43] for more details.

2.2. The structure equations

The motion of an elastic structure in terms of its displacement field ***d*** with respect to a given material reference configuration $\hat{\Omega}_s$ is governed by the elastodynamics equation

$$\rho_s \frac{\partial^2 \boldsymbol{d}}{\partial t^2}-\nabla\cdot\sum\nolimits_s(\boldsymbol{d})=\boldsymbol{g}_s \quad \text{in}\,\hat{\Omega}_s\times(t_0,T), \quad (12)$$

where $\boldsymbol{g}_s$ is the body force which we neglect in the following. We assume that the structure behaves like a linearly elastic, or Hookean, material. Thus, we have:

$$\sum\nolimits_s(\boldsymbol{d})=2\mu_s\boldsymbol{\varepsilon}(\boldsymbol{d})+\lambda_s(\nabla\cdot\boldsymbol{d})\mathbf{I}, \quad (13)$$

Here, $\boldsymbol{\varepsilon}(\boldsymbol{d}) = (\nabla\boldsymbol{d} + (\nabla\boldsymbol{d})^T)/2$ is the strain tensor, μ_s and λ_s are the Lamé constants, that are related to Young's modulus *E* and the Poisson ratio ν_s as follows:

$$\mu_s = \frac{E}{2(1+\nu_s)}, \quad \lambda_s = \frac{E\nu_s}{(1+\nu_s)(1-2\nu_s)}.$$

2.2.1. Discretization—For the time discretization of problem (12), we adopt a method from the family of generalized-α schemes (see, e.g., [44]). Such schemes represent a more stable version of the well-known Newmark method

$$\rho_s \boldsymbol{a}^{n+1} - \nabla \cdot \boldsymbol{\sigma}_s(\boldsymbol{d}^{n+1}) = \mathbf{0}, \quad (14)$$

$$\boldsymbol{d}^{n+1} = \boldsymbol{d}^n + \Delta t \boldsymbol{v}^n + \Delta t^2 \left(\beta \boldsymbol{a}^{n+1} + \left(\frac{1}{2} - \beta \right) \boldsymbol{a}^n \right), \quad (15)$$

$$\boldsymbol{v}^{n+1} = \boldsymbol{v}^n + \Delta t \left(\gamma \boldsymbol{a}^{n+1} + (1-\gamma)\boldsymbol{a}^n \right), \quad (16)$$

where $\boldsymbol{v}^n$ and $\boldsymbol{a}^n$ are proper approximations of the structure velocity and acceleration at time t^n. Here, set $\beta = \frac{1}{4}$ and $\gamma = \frac{1}{2}$ to have second order accuracy. The numerical solutions obtained with the Newmark scheme may be affected by high frequency spurious oscillations if the time step is not small enough compared to the space discretization parameters. Generalized-α methods act as low-pass filters that selectively introduce numerical damping only for the high frequency modes, while conserving the low frequency modes. The spectral properties of those methods are determined by a single parameter: the asymptotic spectral radius ρ_∞ ($0 \le \rho_\infty \le 1$). If $\rho_\infty = 1$ the generalized-α method reduces to the Newmark method. By setting

$$\boldsymbol{a}^{n+1-\alpha_m} = (1-\alpha_m(\rho_\infty))\boldsymbol{a}^{n+1} + \alpha_m(\rho_\infty)\boldsymbol{a}^n, \quad 0 \le \alpha_m(\rho_\infty) \le 1 \quad (17)$$

$$\boldsymbol{d}^{n+1-\alpha_k} = (1-\alpha_k(\rho_\infty))\boldsymbol{d}^{n+1} + \alpha_k(\rho_\infty)\boldsymbol{d}^n, \quad 0 \le \alpha_k(\rho_\infty) \le 1, \quad (18)$$

the generalized-α scheme replaces momentum equation (14) by

$$\rho_s \boldsymbol{a}^{n+1-\alpha_m} - \nabla \cdot \boldsymbol{\sigma}_s(\boldsymbol{d}^{n+1-\alpha_k}) = \mathbf{0}. \quad (19)$$

By using (17)–(18) and (15)–(16), it is possible to rewrite equation (19) in terms of the only unknown $\boldsymbol{v}^{n+1}$. Concerning the particular choice of the generalized-α method and parameters, we take $\alpha_m = -1$, $\alpha_k = 0$, $\gamma = 3/2$ and $\beta = 1$, which correspond to $\rho_\infty = 0$. This scheme, originally proposed in [45], features excellent stability properties and second order of accuracy in time.

For the space discretization, we introduce a conformal and quasi-uniform triangulation $\mathcal{T}_h^s$ of $\hat{\Omega_s}$ made up of a certain number of tetrahedra and we set up a Galerkin finite element procedure using $\mathbb{P}_2$ elements. We denote by M_s the mass matrix and by K_s the stiffness matrix obtained after discretization of problem (12). The problem now becomes: given $\mathbf{v}^n$, for $n \ge 1$, find the solution $\mathbf{v}^{n+1}$ of equation:

$$D\mathbf{v}^{n+1} = \mathbf{b}_s^{n+1}, \quad \text{with} \quad D = \rho_s \frac{1-\alpha_m}{\gamma \Delta t} M_s + (1-\alpha_k)\frac{\beta}{\gamma}\Delta t K_s,$$

where **v** is the array of nodal values for the structure velocity, while $\mathbf{b}_s$ accounts for the contributions of the solution at the previous time steps and boundary conditions.

2.3. The coupled problem

The structure deforms due to the contact force exerted by the fluid onto the fluid-structure interface, so that both the structure and fluid domains depend on *t*, i.e. $\Omega_s = \Omega_s(t)$ and $\Omega_f = \Omega_f(t)$. Let us denote by $\Gamma(t)$ the fluid-structure interface, that is the common boundary between $\Omega_f(t)$ and $\Omega_s(t)$. The fluid problem (1)–(2) and the structure problem (12) are coupled by two transmission conditions:

1. continuity of velocity

$$\boldsymbol{u}=\boldsymbol{v} \quad \text{on}\,\Gamma(t), t_0<t\leq T; \quad (20)$$

2. continuity of stress

$$\boldsymbol{\sigma}_f\boldsymbol{n}=\boldsymbol{\sigma}_s\boldsymbol{n} \quad \text{on}\,\Gamma(t), t_0<t\leq T, \quad (21)$$

n being the outward normal for $\Omega_f(t)$. In (21), $\boldsymbol{\sigma}_s$ is the structure Cauchy stress tensor, which is the Eulerian description of the second Piola-Kirchhoff stress tensor $\boldsymbol{\Sigma}_s$ defined in (13).

In order to describe the evolution of the whole domain $\Omega(t) = \Omega_f(t) \cup \Omega_s(t)$, we adopt two different approaches in each subdomain. The structure domain is described with a Lagrangian mapping as in section 2.2. Thus, if $\boldsymbol{d}$: $\hat{\Omega_s} \times (t_0, T)$ denotes the displacement of the structure with respect to the reference configuration, then each point $\boldsymbol{x}_s$ in the current configuration $\Omega_s(t)$ is associated to a point $\boldsymbol{x}_s\hat{}$ in the reference configuration by $\boldsymbol{x}_s(\boldsymbol{x}_s\hat{}, t) = \boldsymbol{x}_s\hat{} + \boldsymbol{d}(\boldsymbol{x}_s\hat{}, t)$. The fluid domain is described with an *Arbitrary Lagrangian-Eulerian* (ALE) mapping. In other words, its kinematics is only required to comply by that of the boundary $\Gamma(t)$, which is the result of the coupling with the structural model. We define the position $\boldsymbol{x}_f$ of internal points to $\Omega_f(t)$ as the harmonic extension of the position of points on $\Gamma(t)$. See, e.g., [46, 47] for details. The position in the reference fluid domain $\hat{\Omega_f}$ (at $t = 0$) is denoted by $\boldsymbol{x}_f\hat{}$ and the domain velocity $\boldsymbol{w}$ is calculated using the following expression:

$$\boldsymbol{w}(\boldsymbol{x}_f, t)=\frac{\partial \boldsymbol{x}_f}{\partial t}\Big|_{\hat{\boldsymbol{x}}_f}.$$

The velocity ALE time derivative, i.e. rate of change of the fluid velocity in a point that moves with the computational domain reads

$$\frac{\partial \boldsymbol{u}}{\partial t}\Big|_{\hat{\boldsymbol{x}}_f}=\frac{\partial \boldsymbol{u}}{\partial t}+\boldsymbol{w}\cdot\nabla\boldsymbol{u}.$$

With these definitions, we can write the incompressible Navier-Stokes equations in ALE formulation as follows:

$$\rho_f\frac{\partial \boldsymbol{u}}{\partial t}\Big|_{\hat{\boldsymbol{x}}_f}+\rho_f\left(\boldsymbol{u}-\boldsymbol{w}\right)\cdot\nabla\boldsymbol{u}-\nabla\cdot\boldsymbol{\sigma}_f=\boldsymbol{0} \quad \text{in}\,\Omega_f\left(t\right), \quad (22)$$

$$\nabla \cdot \boldsymbol{u}=0 \quad \text{in}\,\Omega_f\,(t), \quad (23)$$

for $t \in (t_0, T)$. Coupling conditions (20),(21) can be written in the equivalent form

$$r_f \boldsymbol{u}+\boldsymbol{\sigma}_f \boldsymbol{n}=r_f \boldsymbol{v}+\boldsymbol{\sigma}_s \boldsymbol{n} \quad \text{on}\,\Gamma(t), \quad (24)$$

$$r_s \boldsymbol{u}+\boldsymbol{\sigma}_f \boldsymbol{n}=r_s \boldsymbol{v}+\boldsymbol{\sigma}_s \boldsymbol{n} \quad \text{on}\,\Gamma(t), \quad (25)$$

where $r_f > 0$ and $r_s > 0$ ($r_f \neq r_s$) are constants.

2.3.1. Discretization—At every time level t^{n+1}, the FSI problem discretized in time and space can be written in matrix form as:

$$A_{fs}\mathbf{x}_{fs}^{n+1}=\mathbf{b}_{fs}^{n+1}, \quad (26)$$

$$A_{fs}=\begin{bmatrix} C+r_f R_f & T_{fs} & B^T \\ T_{su} & D+r_s R_s & T_{sp} \\ B & 0 & 0 \end{bmatrix}, \quad \mathbf{x}_{fs}^{n+1}=\begin{bmatrix} \mathbf{u}^{n+1} \\ \mathbf{v}^{n+1} \\ \mathbf{p}^{n+1} \end{bmatrix}, \quad \mathbf{b}_{fs}^{n+1}=\begin{bmatrix} \mathbf{b}_u^{n+1} \\ \mathbf{b}_s^{n+1} \\ \mathbf{0} \end{bmatrix}. \quad (27)$$

Here, the boundary mass matrices R_f, R_s and the coupling matrices T_{fs}, T_{su}, T_{sp} arise from the discretization of the coupling conditions (24),(25).

To precondition system (26), we consider an inexact *LU* block factorization of the matrix A_{fs}, in a similar way to what already done in Sec. 2.1 and in the same spirit of [46, 47]. The approximated *U* factor for matrix A_{fs} is:

$$\widehat{U}_{fs}=\begin{bmatrix} C+r_f R_f & T_{fs} & B^T \\ 0 & \widehat{\sum}_s & T_{sp} \\ 0 & 0 & \widehat{\sum}_p \end{bmatrix},$$

where $\hat{\Sigma_s}$ and $\hat{\Sigma_p}$ are appropriate approximations of the structure Schur complement

$$\sum\nolimits_s = D+r_s R_s - T_{su}(C+r_f R_f)^{-1} T_{fs},$$

and the pressure Schur complement

$$\sum\nolimits_p = -B(C+r_f R_f)^{-1} B^T + B(C+r_f R_f)^{-1} T_{fs} \sum\nolimits_s^{-1} T_{su}(C+r_f R_f)^{-1} B^T - B(C+r_f R_f)^{-1} T_{fs} \sum\nolimits_s^{-1} T_{sp}.$$

To approximate Σ_s, we use $(C + r_f R_f)^{-1} \approx H$, where H is defined in (10). Thus, we have:

$$\widehat{\sum}_s = D+r_s R_s - T_{su} H T_{fs}$$

To approximate Σ_p, we modify the pressure corrected Yosida preconditioner defined in Sect. 2.1 as follows:

$$\widehat{\sum}_p = S(S + BH(\mu_f K + \rho_f N + r_f R_f)HB^T)^{-1}S. \quad (28)$$

At every time level t^{n+1}, we solve $\widehat{U}_{fs}^{-1} A_{fs} \mathbf{x}_{fs}^{n+1} = \widehat{U}_{fs}^{-1} \boldsymbol{b}_{fs}^{n+1}$ with the GMRES method. The position of the fluid domain is extrapolated from the previous time step, while the non-linearity induced by the fluid convective term is resolved with Picard iterations (see e.g. [37]).

3. RESULTS

3.1. The FDA benchmark

The FDA benchmark consists in simulating the flow of an incompressible and Newtonian fluid with prescribed density and viscosity (ρ_f = 1056 kg/m^3 and μ_f = 0.0035 Pa·s) in an idealized medical device shaped like a nozzle (see Fig. 1) at different Reynolds numbers.

The geometry of the device includes a conical convergent, a throat, and a sudden expansion. In this paper, we are only considering the so-called “Sudden Expansion” model [12, 19], that is in Fig. 1 the fluid flows from left to right. The idealized device was designed to feature accelerating, decelerating, and recirculating flow, all of which occur in real medical devices.

The system is studied in a variety of conditions, including the laminar, transitional, and turbulent regimes: the results of the published inter-laboratory experiments refer to values of the Reynolds numbers (defined as in (3)) evaluated in the throat, denoted by Re_t, of Re_t = 500, 2000, 3500, 5000, 6500. In this paper, we focus on the first three values of Re_t for reasons that will be clarified in the following (see Remark 3.4). In table I, we report the throat Reynolds number Re_t, the corresponding inlet Reynolds number Re_i, and flow rate for the flow regimes that we are going to consider. Notice that in all the three flow regimes the flow upstream of the throat is laminar, Re_i being below the critical Reynolds number for transitional flow in a straight pipe ($Re \simeq 2000$ [48]).

Since we are dealing with a viscous fluid, on the lateral surface of the computational domain we prescribe a no-slip boundary condition. For all three flow regimes in table I, at the inlet section we prescribe a Poiseuille velocity profile to get the desired flow rate, a choice which is justified by the considered values of Re_i. At the outlet section, we prescribe a stress-free (natural) boundary condition. This simulates a discharge into open air, which does not correspond to the experimental set up of the FDA benchmark (a closed flow loop [12]). However, this choice is expected to alter the computed solution only in a confined region of the computational domain close to the outlet section [49]. The results of the flow analysis are not affected, provided the computational domain represents a long enough expansion channel. As discussed in the following, we always considered the length of the expansion channel (L_o in Fig. 1) to be greater than 10 times its diameter, and we did not observe a dependence of the solution on the actual value of L_o.

As for the initial condition, we start our simulations with fluid at rest, i.e., $p = 0$ and $\boldsymbol{u} = \mathbf{0}$ everywhere in Ω_f. We use a smooth increase of the velocity profile at the inlet to transition from the fluid at rest to the regime flow conditions. A short transition reduces the duration and therefore the overall computational cost of the simulation. However, a fine time discretization is required to resolve fast transient dynamics of the computed solution.

For every flow regime, we use direct numerical simulations (DNS), with no turbulence model. This choice is motivated by the results presented in [19], where it is shown that DNS most accurately predicts the velocities at all Re_t, in particular in the entrance region, in the throat, and just downstream of the sudden expansion. In DNS, it is essential to assess whether or not the flow field is properly resolved. For this purpose, we follow the approach proposed by [50], that is the grid resolution is qualified in terms of the viscous length scale, computed as

$$l^+ = \frac{u_* \Delta l}{\nu_f}, \quad \text{with } \Delta l = 12/\sqrt{2} V_\tau^{1/3}, \text{ and } u_*^2 = \nu_f \left|\left|\boldsymbol{\varepsilon}(\boldsymbol{u})\right|\right|_F. \quad (29)$$

In (29), Δl represents the local grid size, V_τ is the tetrahedron volume, and $\| \cdot \|_F$ is the Frobenius norm. If $l^+ \sim O(1)$, the average grid size Δl is of the order of the viscous length scale, which is the smallest spatial scale at which turbulent fluctuation can persist.

As mentioned in Sec. 2.1, selection of the time step was not driven by stability issues but rather based on accuracy considerations solely.

We compare the experimental data provided by the FDA with our numerical simulations for all the flow regimes listed in table I. The experimental data were acquired by three independent laboratories and one of the laboratory ran three trials, so that for each case we have five sets of data. The comparison is made in terms of normalized axial component of the velocity along the centerline and at various radial sections (see Fig. 2), and normalized wall pressure difference along the length of the domain. The axial component of the velocity u_z is normalized with respect to the average axial velocity at the inlet $\bar{u}_i$:

$$u_z^{norm} = \frac{u_z}{\overline{u}_i}, \quad \text{with} \quad \overline{u}_i = \frac{Q}{\pi D_i^2/4}, \quad (30)$$

where Q is the volumetric flow rate calculated from the throat Reynolds number (see table I). The pressure difference data are normalized with respect to the average velocity at the throat $\bar{u}_t$:

$$\Delta p^{norm} = \frac{p_z - p_z = 0}{1/2 \rho_f \overline{u}_t^2}, \quad \text{with} \quad \overline{u}_t = \frac{Q}{\pi D_t^2/4}, \quad (31)$$

where p_z denotes the wall pressure along the z axis and $p_{z=0}$ is the wall pressure at $z = 0$. As a proxy for the wall pressure at a given axial coordinate, we probed the pressure value at the corresponding location on the axis of the domain, since we observed pressure values being approximately uniform on axial cross-sections.

The graphs with the above comparisons are reported in Sec. 3.1.1 for $Re_t = 500$, Sec. 3.1.2 for $Re_t = 2000$, and Sec. 3.1.3 for $Re_t = 3500$. Finally, a quantification of the agreement is provided in Section 3.1.4 following a validation metric proposed in [19].

3.1.1. Case $Re_t = 500$—Among the considered values of Re_t, the case $Re_t = 500$ proved to be the the easiest to be studied, as expected since the flow is laminar all along the length of the domain.

We selected $L_i = 10D_i$ and $L_o = 15D_i$ (see Fig. 1) and considered three meshes with different levels of refinement:

- mesh *coarse15D*, with an average element diameter $h_{avg} = 6.9 \cdot 10^{-4}$, a maximum element diameter $h_{max} = 1.8 \cdot 10^{-3}$ and a minimum element diameter $h_{min} = 1.7 \cdot 10^{-4}$; this mesh has $1.7 \cdot 10^5$ nodes and $8.3 \cdot 10^5$ tetrahedra;
- mesh *medium15D*, with $h_{avg} = 4.5 \cdot 10^{-4}$, $h_{max} = 1.9 \cdot 10^{-3}$, $h_{min} = 1.3 \cdot 10^{-4}$; this mesh has $6.3 \cdot 10^5$ nodes and $3.4 \cdot 10^6$ tetrahedra;
- mesh *fine15D*, with $h_{avg} = 3.4 \cdot 10^{-4}$, $h_{max} = 1.8 \cdot 10^{-3}$, $h_{min} = 9.2 \cdot 10^{-5}$; this mesh has $1.3 \cdot 10^6$ nodes and $7 \cdot 10^6$ tetrahedra.

A special refinement was prescribed, so that the mesh size was reduced in the convergent and h_{min} was achieved in the throat. All three meshes had a small value of the viscous length scale at the steady state (maximum value $l^+ \simeq 0.5$ over the entire domain). We ran a simulation on each mesh, with time step $\Delta t = 10^{-3}$ for every mesh and using $\mathbb{P}_1^b - \mathbb{P}_1$ finite elements. An advantage of this choice of finite elements is that the resulting algebraic problem is significantly smaller and easier to solve with respect to the one generated by choosing $\mathbb{P}_2$-$\mathbb{P}_1$ finite elements. The latter are however more accurate, and this may be required in some cases, as we discuss later.

We let the simulations run until reasonably close to the steady state. To this aim, we monitored the flow rate and average pressures at the inlet and outlet sections. After $t = 3$ s, all the simulations gave a pressure drop along the nozzle with at least four stable significant digits, and a flow rate with at least five stable significant digits. We observed high frequency oscillations in the pressure field computed on the finest mesh, that we attribute to numerical rounding errors magnified by the high condition number of the corresponding matrices. In this case, to isolate the variability due solely to the transient regime we applied a low-pass filter to the sequence of computed values. To reach $t = 3$ s required roughly 15.5 hours of computational time on 32 CPUs for mesh *coarse15D*, 24 hours on 128 CPUs for mesh *medium15D*, 36 hours on 256 CPUs for mesh *fine15D*.

First, we report the comparison for the normalized axial velocity (30) along the z axis (Fig. 3(a)) and the normalized pressure difference (31) along the z axis (Fig. 3(b)). In Fig. 3, we plotted a dot for every measure and a solid line to linearly interpolate the five sets of measurements, while we used a dashed line for the numerical results obtained with the three meshes. From Fig. 3(a), we see that the numerical axial velocities computed on the *medium15D* and *fine15D* meshes are always superimposed, showing that mesh independence is achieved with the second level of refinement. Results obtained on the *coarse15D* mesh are superimposed to the previous in the entrance region, convergent, and throat, while they differ in the sudden expansion region. However, the axial velocities computed on all the meshes are in agreement with the measurements, all along the portion of the z axis under consideration ($-0.088 \le z \le 0.08$). As for the numerical pressure differences, the three curves corresponding to the computational results on the three meshes cannot be distinguished in the scale of the picture, all along the axis (see Fig. 3(b)), but they do not match the measured data. As reported in [19], these data sets seem in fact to be significantly affected by normalization errors. This would explain the apparent positive offset of about 1.5 mmHg in most of the measurements with respect to the computed values. Moreover, the experimental results vary significantly from one data set to the other, suggesting that a comparison with the measurements is troublesome in this case.

In Fig. 4, we show the profiles of the normalized axial velocity (30) at four different radial sections. In the entrance region and in the throat (Fig. 4(a) and (b)) there is no noticeable difference between the numerical results obtained on the different meshes, indicating that no further refinement is required there. In the same pictures, a mismatch is however observed between the numerical velocity profiles and the measurements. Given the velocity profile at

each section and assuming axial symmetry, we can calculate the associated flow rate. By comparing this flow rate with the theoretical flow rate needed to have $Re_t = 500$, we find that the flow rate computed from the measured velocity profiles underestimates the theoretical flow rate by at least 3%, while the flow rate computed from the simulated velocity profiles retrieves the correct value within an error of 0.019% (using the fine mesh). For this reason, we conclude that the mismatch observed in Fig. 4(a) and (b) is due to measurement errors. Downstream of the sudden expansion (Fig. 4(c) and (d)), the simulated velocity profiles on meshes *medium15D* and *fine15D* coincide, they match the experimental data and are able to correctly capture the negative velocities within the recirculation zones. Results obtained on mesh *coarse15D*, although within the range of variability of the experimental data, do not accurately represent the velocity profile. In particular, the velocity profile is not axisymmetric, as can be clearly appreciated on the axis of the nozzle. These results are consistent with those presented in Fig. 3(a).

Remark 3.1: As mentioned in Sec. 3.1, the mesh plays a central role in DNS. At $Re_t = 500$, the flow is axially symmetric for $-0.088 \leq z \leq 0.08$. It is important that the mesh is close to uniform on each axial section to respect the symmetry of the problem. A mesh that does not have such a feature would give unphysical asymmetric velocity profile.

3.1.2. Case $Re_t = 2000$—The transitional regime ($Re_t = 2000$) proved to be a tough test both from the experimental and numerical point of view.

From the experimental side, the interlaboratory velocity data agreed with each other within 15% error at the entrance, convergent, throat, and right after the sudden expansion. However, farther downstream of the sudden expansion the velocity profiles from the laboratories are significantly different from one another. In particular, the experimental jet breakdown point varied among the laboratories. This was attributed mainly to a 10% higher flow rate (and consequently higher Re_t) which caused premature jet breakdown in two experiments out of five [12]. However, minor differences in the fabricated geometrical models and inlet perturbation levels played a role also. From the numerical point of view, we found the results to be very sensitive to mesh size and time step.

We selected $L_i = 10D_i$ and $L_o = 12D_i$ (see Fig. 1). After several numerical experiments, we managed to identify a mesh sufficiently refined in the different regions of the domain: average element diameter $h_{avg} = 7.1 \cdot 10^{-4}$, maximum element diameter $h_{max} = 4.5 \cdot 10^{-3}$ and minumum element diameter $h_{min} = 2.1 \cdot 10^{-4}$. Also in this case the mesh was selectively refined in the convergent and in the throat, where h_{min} was obtained. The final mesh has a total of $4.6 \cdot 10^5$ nodes and $2.5 \cdot 10^6$ tetrahedra.

We set time step $\Delta t = 10^{-4}$ and used $\mathbb{P}_2$-$\mathbb{P}_1$ finite elements. Around time $t = 0.45$ s, the turbulent regime is fully developed. The mesh viscous length scale evaluated at this time has a maximum value $l^+ \simeq 2$ over the entire domain.

We start by reporting the comparison for the normalized axial velocity (30) along the z axis (Fig. 5(a)) and the normalized pressure difference (31) along the z axis (Fig. 5(b)). In Fig. 5, we see that the simulated axial velocities and pressure differences match very well with the sets of data showing a longer jet.

Fig. 6 shows the profiles of the normalized axial velocity (30) at four different radial sections. As for the $Re_t = 500$ case, all the sets of measurements slightly underestimate the axial velocity at $z = -0.064$; see Fig. 6(a). Inside the throat (Fig. 6(b)), the velocity profile is plug-like. The peak velocity found by the simulation is slightly less than the ones found experimentally. In this case, the measured velocity profiles overestimate the theoretical flow

rate by at least 2%, while the simulated velocity profiles underestimate it by 0.41% (See Fig. 9(b)). Immediately downstream of the sudden expansion (Fig. 6(c)), the simulated profiles have peak values that fall within the measurements sets and the recirculation zones are pretty well captured. Section $z = 0.06$ (Fig. 6(d)) is close to the jet breakdown point for three sets of measurements, while it is past the breakdown point for the other two sets. The simulated velocity is closer to the former, as already seen in Fig. 5(a).

Remark 3.2: The $\mathbb{P}_1^b-\mathbb{P}_1$ finite elements, which performed well for $Re_t = 500$, failed to give results comparable to the experimental data for $Re_t = 2000$. In the simulation at $Re_t = 2000$ with a mesh and time step similar to those used for the results in Fig. 5 and 6, the $\mathbb{P}_1^b-\mathbb{P}_1$ finite elements gave a numerical jet breakdown point much farther downstream than observed in the experiments. A possible cause of the mismatch with the experimental data is the accuracy of the numerical integration performed by LifeV. $\mathbb{P}_1^b-\mathbb{P}_1$ finite elements require the accurate evaluation of the integral of high order polynomials on the computational domain. The use of numerical methods unable to guarantee the desired accuracy may have caused the artificial damping of high frequency modes in the solution and consequently enhanced its laminar behavior. It is however worth pointing out that the introduction of high order quadrature formulas may significantly affect the computational costs.

3.1.3. Case $Re_t = 3500$—The third flow regime we consider features a throat Reynolds number $Re_t = 3500$ which is well above the transitional Reynolds number in a straight channel. In fact, turbulence downstream of the sudden expansion was observed in all the experiments with a reproducible jet breakdown point, which indicates a fully turbulent flow regime.

We selected $L_i = 10D_i$ and $L_o = 15D_i$ (see Fig. 1). After numerical studies in the throat-expansion region and convergent-throat-expansion region, we managed to identify a sufficient level of refinement for the different regions of the domain. The final mesh has average element diameter $h_{avg} = 8.4 \cdot 10^{-4}$, maximum element diameter $h_{max} = 2.5 \cdot 10^{-3}$, minumum element diameter $h_{min} = 1.4 \cdot 10^{-4}$ for a total of $5.6 \cdot 10^5$ nodes and $3.2 \cdot 10^6$ tetrahedra.

We set time step $\Delta t = 10^{-4}$ and used $\mathbb{P}_2$-$\mathbb{P}_1$ finite elements. Already around time $t = 0.4$ s, the turbulent regime is fully developed. The mesh viscous length scale evaluated at this time has a maximum value $l^+ \simeq 4$ over the entire domain. The simulation of 0.4 s of flow took 336 hours on 256 CPUs.

In [19], none of the presented CFD results was able to catch the jet breakdown point, because DNS predicted a longer jet (likely due to a coarse mesh) while simulations with turbulence models under-predicted the jet length. In Fig. 7(a), we see that DNS with a properly refined mesh is able to capture with precision the jet breakdown observed in the experiments. Actually, the simulated axial velocities matched with the measurements all along the portion of the z axis under consideration. As shown in Fig. 7(b), also the simulated pressure difference is in very good agreement with the experimental data, except in the convergent where the simulated pressure difference overestimates almost all the measurements.

Fig. 8 shows the profiles of the normalized axial velocity (30) at four different radial sections. The velocity profile upstream of the throat (Fig. 8(a)) is of Poiseuille type, as expected (see Re_i in table I). The simulation results are in very good agreement in particular with one of the five data sets. Inside the throat (Fig. 8(b)), the velocity profile is plug-like.

As for Re_t = 2000, the peak velocity found by the simulation is a little lower than the ones found experimentally. Immediately downstream of the sudden expansion (Fig. 8(c)), the velocity profile still shows a plateau and recirculation zones appear. Here, the simulated profile has a peak that falls within the measurements sets, whereas the measurements and numerical results differ at the recirculation zones. However, it was noted in [19] that measuring velocities accurately at the wall is very hard, especially in recirculation zones downstream of the sudden expansion where velocities near the wall are low. Any conclusion about the accuracy of numerical results in that region, drawn by comparison with experimental data, has to be considered purely speculative. Section z = 0.06 (Fig. 8(d)) is past the jet breakdown point, thus the axial component of the velocity is much reduced. The simulated velocity captures well the magnitude of measured velocity and part of the profile.

Remark 3.3: Since the measurements of a turbulent flow are averaged over time [12], we averaged the numerical results. All the results presented in Fig. 7 and 8 have been averaged over 10 time steps. We noticed that averaging over more than 10 would not change the average value.

Remark 3.4: Using DNS has a major limitation in the high computational costs. To fully resolve the flow features at high Reynolds number, it is necessary to consider simulations with a huge number of degrees of freedom [51]. Since the tests that we presented so far already show that our computational framework can simulate adequately flow in laminar, transitional and turbulent regimes, we limit our analysis of the FDA problem to Reynolds number $Re_t \leq 3500$. Possible alternatives to DNS are represented by filtering techniques such as the ones considered in Large Eddy Simulations - see, e.g., [52, 53, 54]. In the future we plan to work on those models to reduce the computational costs of flow simulations in the turbulent regime.

3.1.4. Quantitative analysis—In order to quantify the agreement between the results of a simulation and the experimental data, in [19] a generic validation metric E_z was proposed

$$E_z = \frac{1}{n}\sum_{i=1}^{n}\left|\frac{\overline{u}_{e,i} - u_{c,i}}{\overline{u}_{e,i}}\right|, \quad (32)$$

where $\bar{u}_{e,i}$ is the average of the experimental velocity data at one discrete point i along the z axis, $u_{c,i}$ is the computational data at the same point i, and n is the total number of discrete points.

In tables II and III, we report validation metric E_z (32) at each of the twelve radial sections in Fig. 2 taken separately for Re_t = 500, 2000, 3500. The corresponding graphs in semi-logarithmic scale are shown in Fig. 9(a). For Re_t = 500, the numerical results obtained with mesh *fine15D* were considered (see Sec. 3.1.1).

From Fig. 9(a), we see that in the Re_t = 500 case the value of E_z decreases in the entrance region and in the throat, while it increases (not monotonically) in the expansion region, the maximum value being 0.3941 at z = 0.08 (see table III). In the entrance region and in the throat, E_z for Re_t = 2000 is comparable to the one for Re_t = 500. The value of E_z increases downstream of the sudden expansion, with maximum value equal to 2.0609 at z = 0.06. This large value is mainly due to substantial inter laboratory variations (see Fig. 6(d)). In the Re_t = 3500 case, we see that the value of E_z is low in the entrance region. Then, it increases by nearly two orders of magnitude immediately downstream of the sudden expansion, with maximum value equal to 1.0648 at z = 0.016. It is worth stressing that a large value of E_z does not necessarily reflect a significant discrepancy between computations and

measurements: Fig. 8(c) shows that the computed and measured velocity values at $z = 0.016$ are closer than suggested by the metric. Since the metric is a sum of normalized absolute values, the error is in general large in low-velocity regions such as recirculation zones. In this sense, validation metric (32) may be not the best possible. Nonetheless, we decided to show how our results perform in this metric, so that we can more directly compare our results with the results in [19]. This direct comparison allows us to conclude that the results presented in Sec. 3.1.1, 3.1.2, and 3.1.3 are in excellent agreement with the measurements.

For all the simulations, we evaluated also the conservation of mass at the axial positions z in Fig. 2 using the conservation of mass error metric proposed by [19], that is:

$$E_Q = \frac{Q_{CFD} - Q}{Q} \cdot 100, \quad (33)$$

where Q_{CFD} is the volumetric flow rate computed from the numerical axial velocity profiles. Higher values of this metric identify worse performances of the computational model.

Fig. 9(b) shows the conservation of mass error metric as a a function of z for $Re_t = 500$, 2000, 3500. For $Re_t = 500$, the maximum error is less than 0.06%, which appears to be excellent when compared to the results reported in [19]. Thanks to the fact that the simulation on mesh *fine15D* features good mass conservation properties, we are confident that the simulated pressures in Fig. 3(b) are not far from the real pressures despite the mismatch with the experimental data. For $Re_t = 2000$, largest error (in absolute value) is inside the convergent. There, the mesh quality seems to be the key responsible, as we systematically observe some stretched elements around $z = -0.048$ in our meshes. The combination of stretched mesh elements with finite elements that are only weakly divergence-free (like the $\mathbb{P}_2 - \mathbb{P}_1$ elements we used, [55]) results in a poor approximation of the flow rate locally. Nonetheless, notice that the local validation metric E_z at $z = -0.048$ (see table II) is satisfactory. For $Re_t = 3500$, the error (in absolute value) is below 0.3% on the whole domain. Also in this case though, we observed stretched elements in the convergent and the mesh could not be significantly improved without drastically increasing the number of degrees of freedom. A more careful mesh design seems to be required in regions of the domain featuring axial tapering.

3.2. The Greenshields-Weller numerical benchmark

The numerical fluid-structure interaction benchmark we are going to consider is taken from a paper by Greenshields and Weller [20]. It deals with the propagation of a pressure wave in a fluid-filled elastic tube. The geometry is selected to be representative of blood flow in large arteries: it is a straight cylindrical pipe with circular section, with length $L = 10$ cm, diameter $D = 2$ cm, and a shell of thickness $h_s = 0.2$ cm (see Fig. 10(a)).

The motion of the fluid filling the deformable tube is described by the incompressible Navier-Stokes equations in ALE formulation (22)–(23), with $\rho_f = 1000$ kg/m^3 and $\mu_f = 0.004$ Pa·s. The motion of the elastic shell is described by the elastodynamics equations (12), with $\mu_s = 5.77 \cdot 10^5$ Pa and $\lambda_s = 3.85 \cdot 10^5$ Pa (correspondingly, $E = 10^5$ Pa and $\nu_s = 0.3$). The coupled fluid-structure system is initially at rest and the wave propagation is initiated by setting $p = 500$ Pa at the fluid domain inlet for all $t > 0$. At the fluid domain outlet and on the outer structure wall, a stress-free boundary condition is imposed. Axial movements of the structure are prevented by prescribing a zero velocity in the axial direction on the inlet section.

The pressure step applied at the inlet causes a pressure wave to propagate down the tube. This induces a radial motion of the elastic structure, that shows a time history of damped

oscillations around an asymptotic steady state. The frequency f of the oscillations and the steady state value of the radial displacement $\bar{d}_r$ can be quantified as

$$f=\frac{1}{2\pi}\sqrt{\frac{4E}{D^2\rho_s(1+M_{fs})}},\quad \bar{d}_r=\frac{D^2p}{4Eh_s}.$$

In the definition of f we use the ratio of equivalent fluid mass to solid mass M_{fs}, that depends on the mass of fluid contributing to the radial motion. For the problem at hand, we assume that only a fraction of the fluid mass contributes to the radial motion, and we set $M_{fs} = D/(8h_s)\,\rho_f/\rho_s$ [20]. This value for the equivalent mass assumes a linear distribution of the radial fluid velocity. Finally, we obtain $M_{fs} = 1.67$, $f = 106.1$ Hz and $\bar{d}_r = 0.25$ mm.

An analytical solution for wave speed c can be given as a function of the geometric features, fluid and structure physical parameters of the system:

$$c=\varphi\sqrt{\frac{K_f}{\rho_f}\left[1+\left(\frac{(D+2h_s)^2}{h_s(D+h_s)}-2(1-\nu_s)\right)\frac{K_f}{E}\right]^{-1}},\quad (34)$$

with

$$\varphi=\sqrt{1-\nu_s^2\left[1+\frac{E}{K_f}\frac{h_s}{D}\left(1-\frac{K_f}{E}\frac{\rho_s}{\rho_f}\right)\right]^{-1}}.$$

To the purpose of finding an analytical solution, the fluid was considered slightly compressible, with bulk modulus $K_f = 2.2 \cdot 10^9$ Pa. For the test case, $\phi = 0.95$ and $c = 2.77$ m/s.

The velocity of the fluid along the tube axis is predicted by Joukowsky's equation [56]

$$u_x=\frac{p}{\rho_f c}$$

where p is the pressure gradient. In the case at hand $u_x = 18.02$ cm/s.

We present the comparison between the computed and analytical solutions of the proposed benchmark problem, evaluating the mismatch with respect to each quantity of interest. Following [20], we perform a series of numerical experiments, incrementally reducing the mesh size in the radial and axial directions. We identify the different meshes with a triplet of numbers, corresponding to the number of subdivisions in the axial direction, in the radial direction within the fluid domain, and in the thickness of the tube wall. We construct four meshes with the software GMSH, guaranteeing axial symmetry of the position of the mesh nodes. Each mesh contains an unstructured region, bounded by a cylinder of radius 1cm; outside that cylinder the mesh is structured, and the number of subdivisions in the circumferential direction is such that mesh elements at the interface between the structured and unstructured regions have a small shape factor (see Fig. 10(b)). Here follows the list of considered meshes:

- mesh *20-10-2*, yielding a total number of degrees of freedom of about $1.5 \cdot 10^3$.
- mesh *30-20-3*, yielding a total number of degrees of freedom of about $3.2 \cdot 10^3$.
- mesh *50-30-5*, yielding a total number of degrees of freedom of $1.2 \cdot 10^6$.
- mesh *70-40-7*, yielding a total number of degrees of freedom of about $2.9 \cdot 10^6$.

To compare the computed features of the propagating wave with the theoretical predictions, we limit our analysis to a time interval in which we can neglect the effects of reflected pressure waves from the outlet section. This limitation can be in principle removed, for instance by devising non-reflective boundary conditions (see e.g. [57]). However, we did not investigate this. As shown in Fig. 11, the wave has reached the outlet section at $t = 20$ ms. We therefore consider the results of our numerical experiments only in the time range $t \in (0, 20)$ ms.

Fig. 12 shows the time history of the radial displacement of the structure computed with the finest mesh. The oscillations tend to damp to a constant steady state close to the value predicted by the analytical solution ($\simeq 0.25$ mm).

To compute the average pressure wave speed we first define the wave front at the half-height of the pressure step, or 250 Pa (see [20]); then we fit a first order polynomial to the position of the wave front in the time range $t \in (0, 20)$ ms and compute its (constant) derivative. The resulting estimate is not sensitive to the mesh size (see Fig. 13), and approximates the exact value of 2.77 m/s within a 1% error margin. Table IV shows the predicted wave speed from different numerical simulations with different grid sizes.

As a measure of the half-period of the wave we consider the distance between the first peak and the first valley in the pressure time plot. From the results obtained on the finest mesh we obtain for this value an estimate of 26 mm. Knowing the wave speed, we compute the wave frequency as 106.5 Hz, within 1% error from the analytical prediction.

We noted before that the theoretical value for the wave frequency depends on M_{fs}. The validity of our choice of M_{fs} can be checked on the computed results. Consistently with our assumption, Fig. 14 (a) shows in fact that the radial velocity of the fluid is a linear function of the radial position on a cross section at abscissa 5 cm, apart from a thin layer close to the wall (radius larger than 0.8 cm).

Finally, the axial velocity of the fluid, evaluated on the tube axis, is also a good approximation of the value predicted by Joukowsky's equation, as shown in Fig. 14 (b).

4. CONCLUSIONS

The main goal of this work is to describe an open source framework for the solution of flow problems relevant to biomechanics. At the core of this framework we place the software tools that we use to build the computational mesh (*pre-processing* phase); LifeV, the library of algorithms and data structures that we use to solve the differential problems (*processing* phase); software for the *postprocessing* of the results of the numerical experiments.

Crucial aspects for a CFD framework are its *verification* and *validation*. We show in this paper how our tools can be tested against published benchmark problems for flow in rigid and deformable domains. Within this context, we also believe that it is important to provide a detailed account on the methods that we used, discussing where possible their merits and shortcomings.

In the simulation of flow in transitional and turbulent regimes, we addressed the issue of accuracy in the numerical integration performed by our code, pointing out the potential dramatic effect on the quality of the solution. The importance of the mesh has also been discussed, in particular its consistency with the symmetry of the physical problem. The flexibility of the mesh generator is therefore a key factor. Computational costs have been shown to be significant, as expected, in particular for flow regimes characterized by high values of the Reynolds number. While this is not an intrinsic limitation of the proposed framework, it is certainly an area of possible improvement, for instance through the implementation of effective turbulence models.

An important outcome of this work is the production of a suite of scripts and codes that are based on a completely open-source set of tools, and therefore can be readily shared with the community. As a matter of fact, we will prepare a distribution of our software that will be published through the web portal www.lifev.org and will allow the reproduction of the results presented in this paper.

Acknowledgments

This work has been partly supported by NSF through grant DMS-1109189. Passerini has been partially supported by NIH grant R01 HL70531. This work used the Extreme Science and Engineering Discovery Environment (XSEDE), which is supported by National Science Foundation grant number OCI-1053575. The authors wish to acknowledge technical support and access to computing resources provided by the Texas Learning and Computation Center and the Texas Tech University's High Performance Computing Center (HPCC). The authors wish to thank Prof. R. Glowinski for his advice on this project.

References

1. Taylor, CA.; Steinman, DA. Image-based modeling of blood flow and vessel wall dynamics: applications, methods and future directions. Annals of biomedical engineering; Sixth International Bio-Fluid Mechanics Symposium and Workshop; March 28–30, 2008; Pasadena, California . Mar. 2010 p. 1188-1203.
2. Formaggia, L.; Quarteroni, A.; Veneziani, A. Cardiovascular Mathematics*Modeling, Simulation and Applications*. Vol. 1. Springer; 2009.
3. Galdi, GP.; Rannacher, R.; Robertson, AM.; Turek, S. Hemodynamical Flows. Delhi Book Store; 2008.
4. Hassan T, Ezura M, Timofeev EV, Tominaga T, Saito T, Takahashi A, Takayama K, Yoshimoto T. Computational simulation of therapeutic parent artery occlusion to treat giant vertebrobasilar aneurysm. AJNR American journal of neuroradiology. Jan; 2004 25(1):63–68. [PubMed: 14729530]
5. Whitehead KK, Pekkan K, Kitajima HD, Paridon SM, Yoganathan AP, Fogel MA. Nonlinear power loss during exercise in single-ventricle patients after the Fontan: insights from computational fluid dynamics. Circulation. Sep; 2007 116(11 Suppl):I165–71. [PubMed: 17846299]
6. Marsden AL, Vignon-Clementel IE, Chan FP, Feinstein JA, Taylor CA. Effects of exercise and respiration on hemodynamic efficiency in CFD simulations of the total cavopulmonary connection. Annals of biomedical engineering. Feb; 2007 35(2):250–263. [PubMed: 17171509]
7. Nobili M, Morbiducci U, Ponzini R, Del Gaudio C, Balducci A, Grigioni M, Maria Montevecchi F, Redaelli A. Numerical simulation of the dynamics of a bileaflet prosthetic heart valve using a fluid-structure interaction approach. Journal of Biomechanics. Aug; 2008 41(11):2539–2550. [PubMed: 18579146]
8. Appanaboyina S, Mut F, Lohner R, Putman CM, Cebral JR. Computational fluid dynamics of stented intracranial aneurysms using adaptive embedded unstructured grids. International Journal for Numerical Methods in Fluids. Jan.2008 57:475–493.
9. Pant S, Bressloff NW, Forrester AIJ, Curzen N. The influence of strut-connectors in stented vessels: a comparison of pulsatile flow through five coronary stents. Annals of biomedical engineering. May; 2010 38(5):1893–1907. [PubMed: 20177782]

10. Wu J, Paden BE, Borovetz HS, Antaki JF. Computational fluid dynamics analysis of blade tip clearances on hemodynamic performance and blood damage in a centrifugal ventricular assist device. Artificial organs. May; 2010 34 (5):402–411. [PubMed: 19832736]
11. Fiore GB, Morbiducci U, Ponzini R, Redaelli A. Bubble tracking through computational fluid dynamics in arterial line filters for cardiopulmonary bypass. ASAIO journal (American Society for Artificial Internal Organs: 1992). Sep; 2009 55(5):438–444. [PubMed: 19730002]
12. Hariharan P, Giarra M, Reddy V, Day S, Manning K, Deutsch S, Stewart S, Myers M, Berman M, Burgreen G, et al. Multilaboratory Particle Image Velocimetry analysis of the FDA benchmark nozzle model to support validation of Computational Fluid Dynamcis simulations. J Biomech Engrg. 2011; 133:041 002.
13. Einarsson, B., editor. Software, Environments and Tools. SIAM: Linköping University; Linköping, Sweden: 2005. Accuracy and Reliability in Scientific Computing.
14. FDA's Critical Path Initiative. http://www.fda.gov/ScienceResearch/SpecialTopics/CriticalPathInitiative/ucm07
15. Computational Fluid Dynamics: An FDA's Critical Path Initiative. https://fdacfd.nci.nih.gov/
16. Turek, S.; Schäfer, M. Benchmark computations of laminar flow around cylinder. In: Hirschel, E., editor. Flow Simulation with High-Performance Computers II. Notes on Numerical Fluid Mechanics. Vol. 52. Vieweg: 1996.
17. Turek, S.; Hron, J. Fluid-Structure Interaction Modelling, Simulation, Optimisation, Lecture Notes in Computational Science and Engineering. Vol. 53. Springer; Berlin: 2006. Proposal for numerical benchmarking fluid-structure interaction between an elastic object and laminar incompressible flow.
18. Turek, S.; Hron, J.; Razzaq, M.; Wobker, H.; Schäfer, M. Numerical benchmarking of fluid-structure interaction: A comparison of different discretization and solution approaches. In: Bungartz, HJ.; Mehl, M.; Schäfer, M., editors. Fluid-Structure Interaction II: Modelling, Simulation, Optimisation, Lecture Notes in Computational Science and Engineering. Vol. 73. Springer; 2010. p. 413-424.
19. Stewart S, Paterson E, Burgreen G, Hariharan P, Giarra M, Reddy V, Day S, Manning K, Deutsch S, Berman M, et al. Assessment of CFD performance in simulations of an idealized medical device: Results of FDA's first computational inter laboratory study. Cardiovascular Engineering and Technology. 2012; 3(2):139–160.
20. Greenshields C, Weller H. A unified formulation for continuum mechanics applied to fluid-structure interaction in flexible tubes. Int J Numer Methods Eng. 2005; 64:1575–1593.
21. LifeV - A parallel Finite Element library. www.lifev.org
22. Heroux MA, Bartlett RA, Howle VE, Hoekstra RJ, Hu JJ, Tamara GK, Lehoucq RB, Long KR, Pawlowski RP, Phipps ET, et al. An overview of the trilinos project. ACM Trans Math Softw. 2005; 31(3):397–423. http://doi.acm.org/10.1145/1089014.1089021.
23. Gauthier A, Saleri F, Veneziani A. A Fast Preconditioner for the Incompressible Navier Stokes Equations. Computing and Visualization in Science. 2004; 6(2):105–112.
24. Fernandez MA, Moubachir M. A Newton method using exact jacobians for solving fluid-structure coupling. Computers and Structures. 2005; 83(2–3):127–142.
25. Formaggia L, Moura A, Nobile F. On the stability of the coupling of 3D and 1D fluid-structure interaction models for blood flow simulations. RAIRO-M2AN Modelisation Math et Analyse Numerique-Mathem Modell Numerical Analysis. 2007; 41(4):743–769.
26. Gerardo-Giorda L, Mirabella L, Nobile F, Perego M, Veneziani A. A model-based block-triangular preconditioner for the bidomain system in electrocardiology. Journal Of Computational Physics. 2009; 228(10):3625–3639.
27. Crosetto P, Deparis S, Fourestey G, Quarteroni A. Parallel algorithms for fluid-structure interaction problems in haemodynamics. SIAM Journal on Scientific Computing. 2010; 33(4):1598–1622.
28. Malossi ACI, Blanco PJ, Deparis S, Quarteroni A. Algorithms for the partitioned solution of weakly coupled fluid models for cardiovascular flows. Int J Num Meth Biomed Engng. 2011; 27(12):2035–2057.
29. Vergara C, Zunino P. Multiscale boundary conditions for drug release from cardiovascular stents. Multiscale Modeling & Simulation. 2008:565–588.

30. Corno AF, Prosi M, Fridez P, Zunino P, Quarteroni A, von Segesser LK. The non-circular shape of FloWatch-PAB prevents the need for pulmonary artery reconstruction after banding. Computational fluid dynamics and clinical correlations. European journal of cardio-thoracic surgery: official journal of the European Association for Cardio-thoracic Surgery. 2006; 29:93–9. [PubMed: 16337404]
31. Ponzini R, Vergara C, Redaelli A, Veneziani A. Reliable CFD-based estimation of flow rate in haemodynamics measures. Ultrasound in medicine & biology. Oct; 2006 32(10):1545–1555. [PubMed: 17045876]
32. Mirabella L, Haggerty CM, Passerini T, Piccinelli M, Powell AJ, Del Nido PJ, Veneziani A, Yoganathan AP. Treatment planning for a TCPC test case: A numerical investigation under rigid and moving wall assumptions. International Journal For Numerical Methods In Biomedical Engineering. Sep.2012 Published online. 10.1002/cnm.2517
33. Passerini T, Sangalli LM, Vantini S, Piccinelli M, Bacigaluppi S, Antiga L, Boccardi E, Secchi P, Veneziani A. An Integrated Statistical Investigation of Internal Carotid Arteries of Patients Affected by Cerebral Aneurysms. Cardiovascular Engineering and Technology. 2012; 3(1):26–40.
34. Schöberl, J.; Gerstmayr, H.; Gaisbauer, R. NETGEN - automatic mesh generator. 2012. http://www.hpfem.jku.at/netgen
35. Geuzaine C, Remacle J. Gmsh: a three-dimensional finite element mesh generator with built-in pre-and postprocessing facilities. Int J Numer Meth Engng. 2009; 79:1309–1331.
36. Henderson, A. ParaView Guide, A Parallel Visualization Application. 2007. http://www.paraview.org
37. Quarteroni, A.; Sacco, R.; Saleri, F. Numerical Mathematics. Springer Verlag; 2007.
38. Quarteroni, A.; Valli, A. Numerical Approximation of Partial Differential Equations. Springer-Verlag; 1994.
39. Saleri F, Veneziani A. Pressure Correction Algebraic Splitting Methods for the Incompressible Navier-Stokes Equations. SIAM Journal on Numerical Analysis. 2006; 43(1):174–194.
40. Quarteroni A, Saleri F, Veneziani A. Analysis of the Yosida method for the incompressible Navier-Stokes equations. J Math Pures Appl. 1999; 78:473–503.
41. Quarteroni A, Saleri F, Veneziani A. Factorization methods for the numerical approximation of Navier-Stokes equations. Comput Methods Appl Mech Engrg. 2000; 188:505–526.
42. Gervasio P, Saleri F, Veneziani A. Algebraic fractional-step schemes with spectral methods for the incompressible Navier-Stokes equations. J Comp Phys. 2006; 214(1):347–365.
43. Villa, U. PhD Thesis. Emory University; 2012. Scalable efficient methods for incompressible fluid-dynamics in engineering problems.
44. Erlicher S, Bonaventura L, Bursi OS. The analysis of the generalized-α method for non-linear dynamic problems. Computational Mechanics. 2002; 20:83–104.
45. Wood WL, Bossak M, Zienkiewicz OC. An alpha modification of Newmarks method. Int J Numer Meth Eng. 1981; 15:1562–1566.
46. Quaini A, Quarteroni A. A semi-implicit approach for fluid-structure interaction based on an algebraic fractional step method. Math Model Meth Appl Sci. 2007; 17(6):957–983.
47. Badia S, Quaini A, Quarteroni A. Splitting methods based on algebraic factorization for fluid-structure interaction. SIAM J Sci Comp. 2008; 30(4):1778–1805.
48. Reynolds O. An experimental investigation of the circumstances which determine whether the motion of water shall be direct or sinuous and of the law of resistance in parallel channels. Proc R Soc Lond Ser. 1883; 35:84–99.
49. Heywood J, Rannacher R, Turek S. Artificial Boundaries and Flux and Pressure Conditions for the Incompressible Navier-Stokes Equations. International Journal for Numerical Methods in Fluids. Jan.1996 22:325–352.
50. Valen-Sendstad K, Mardal KA, Mortensen M, Reif BAP, Langtangen HP. Direct numerical simulation of transitional flow in a patient-specific intracranial aneurysm. J Biomech. 2011; 44:2826–2832. [PubMed: 21924724]
51. Tran CV. The number of degrees of freedom of three-dimensional Navier–Stokes turbulence. Physics of Fluids. Dec.2009 21(12)

52. Layton W, Rebholz L, Trenchea C. Modular nonlinear filter stabilization of methods for higher Reynolds numbers flow. J Math Fluid Mech. 2012; 14(2):325–354.

53. Bowers A, Rebholz L, Takhirov A, Trenchea C. Improved accuracy in regularization models of incompressible flow via adaptive nonlinear filtering. Int J Numer Meth Fluids. 2012; 70:805–828.

54. Layton, WJ.; Rebholz, LG. Lecture Notes in Mathematics. Vol. 2042. Springer; 2012. Approximate Deconvolution Models of Turbulence: Analysis, Phenomenology and Numerical Analysis.

55. Brezzi, F.; Fortin, M. Mixed and Hybrid finite element method. Springer-Verlag; Berlin: 1991.

56. Joukowsky N. Über den hydraulischen Stoss in Wasserleitungsröhren. (On the hydraulic hammer in water supply pipes.). Mémoires de l'Académie Impériale des Sciences de St-Pétersbourg (1900), Series 8. 9(5):1–71. (In German).

57. Formaggia L, Gerbeau JF, Nobile F, Quarteroni A. On the coupling of 3D and 1D Navier-Stokes equations for flow problems in compliant vessels. Comput Methods Appl Mech Engrg. 2001; 191(6–7):561–582.

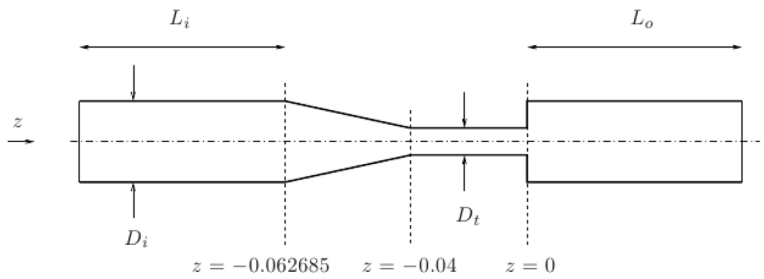

Figure 1.
Computational domain. The units are meter.

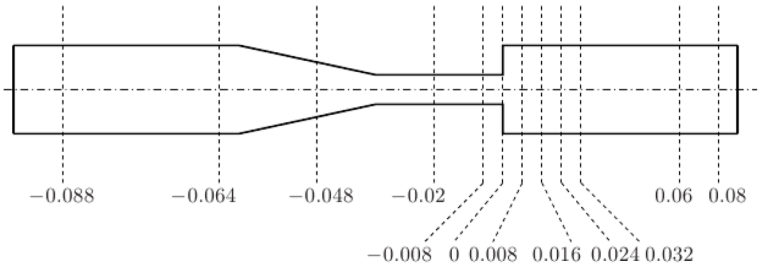

Figure 2.
Radial sections at which the numerical results are compared against the experimental measurements.

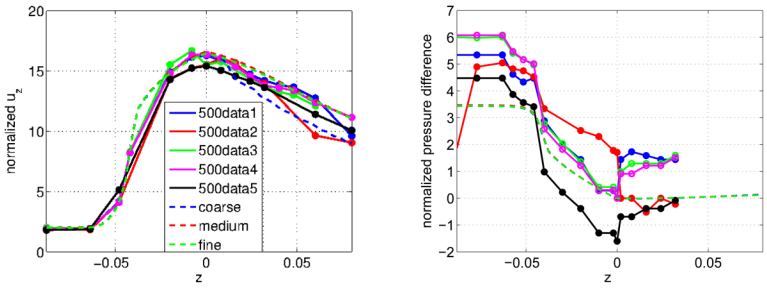

(a) normalized axial velocity along z (b) normalized pressure difference along z

Figure 3.

Case Re_t = 500: comparison between experimental data (solid lines) and numerical results (dashed lines) for (a) normalized axial velocity (30) along the z axis and (b) normalized pressure difference (31) along the z axis. The legend in (a) is common to the two subfigures.

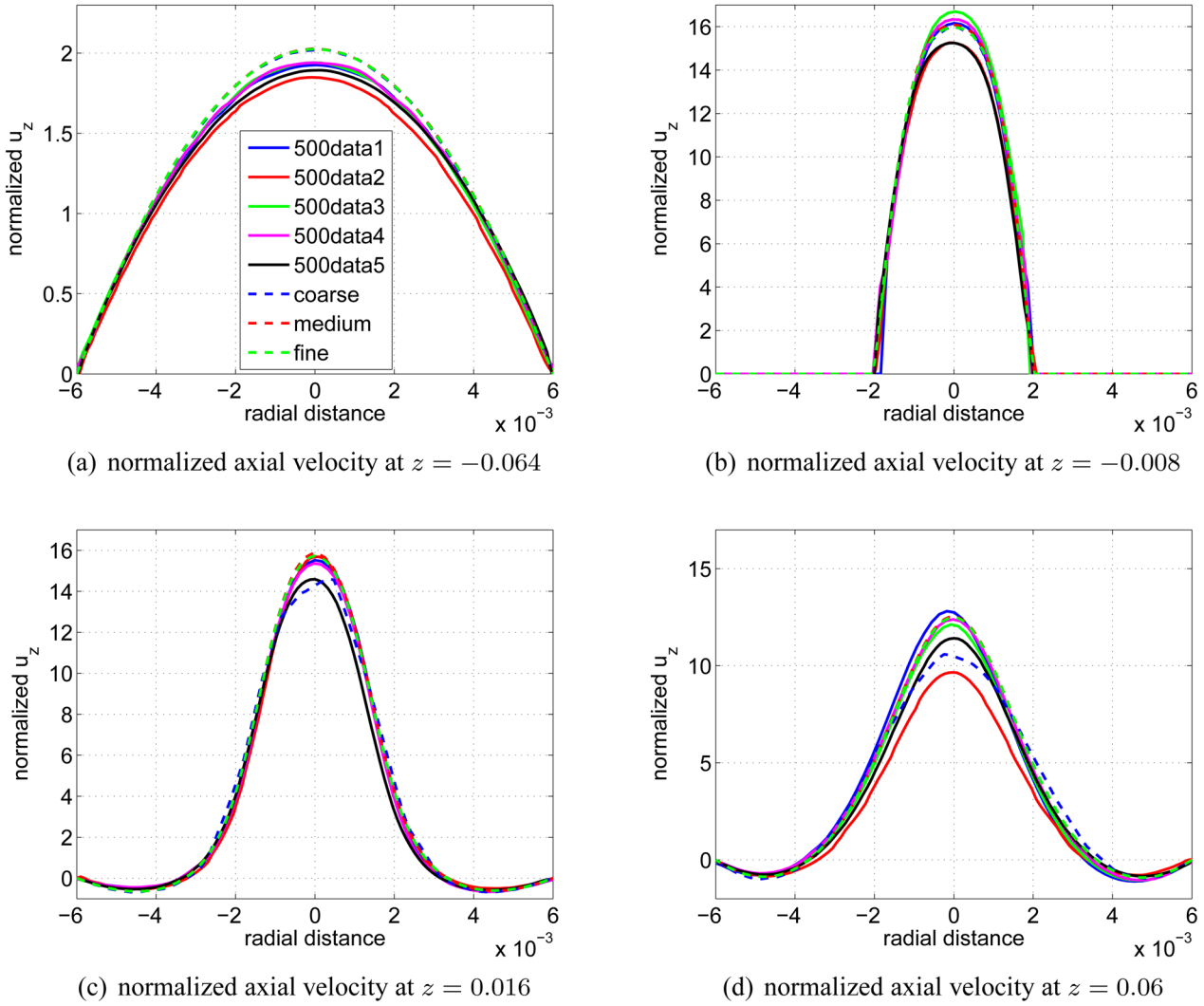

(a) normalized axial velocity at $z = -0.064$

(b) normalized axial velocity at $z = -0.008$

(c) normalized axial velocity at $z = 0.016$

(d) normalized axial velocity at $z = 0.06$

Figure 4.

Case Re_t = 500: comparison between experimental data (solid lines) and numerical results (dashed lines) for normalized axial velocity (30) at (a) z = −0.064, (b) z = −0.008, (c) z = 0.016, and (d) z = 0.06. The legend in (a) is common to all four subfigures.

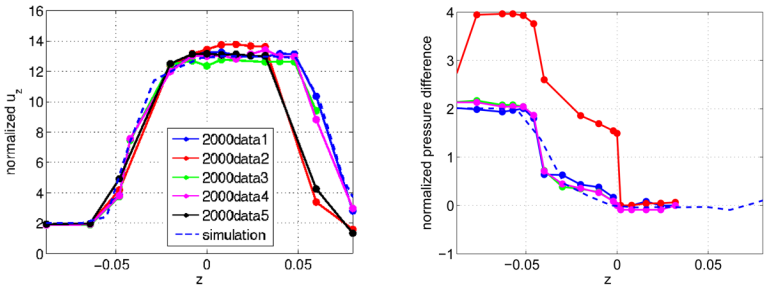

(a) normalized axial velocity along z (b) normalized pressure difference along z

Figure 5.

Case Re_t = 2000: comparison between experimental data (solid lines) and numerical results (dashed line) for (a) normalized axial velocity (30) along the z axis and (b) normalized pressure difference (31) along the z axis. The legend in (a) is common to both subfigures.

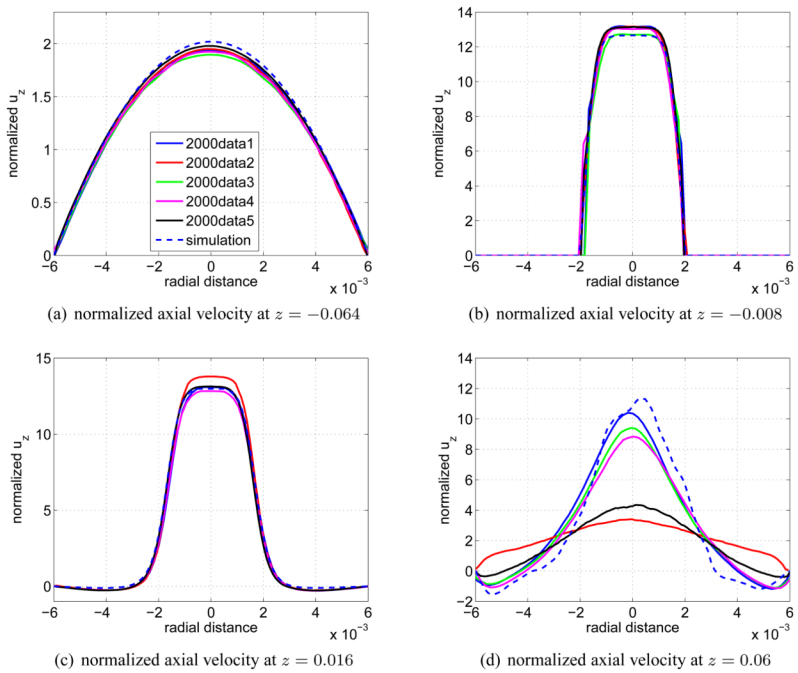

Figure 6.

Case Re_t = 2000: comparison between experimental data (solid lines) and numerical results (dashed line) for normalized axial velocity (30) at (a) z = −0.064, (b) z = −0.008, (c) z = 0.016, and (d) z = 0.06. The legend in (a) is common to all four subfigures.

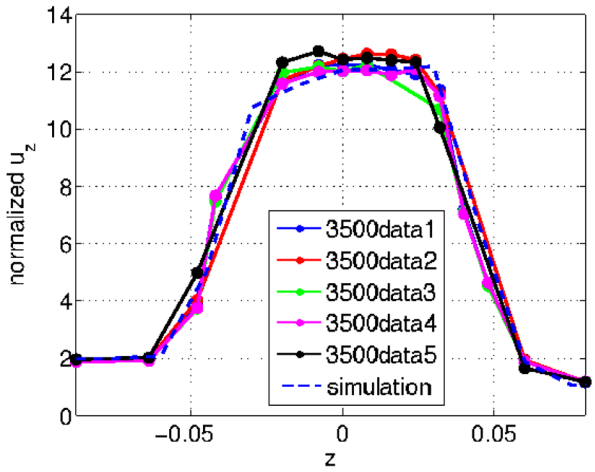

(a) normalized axial velocity along z

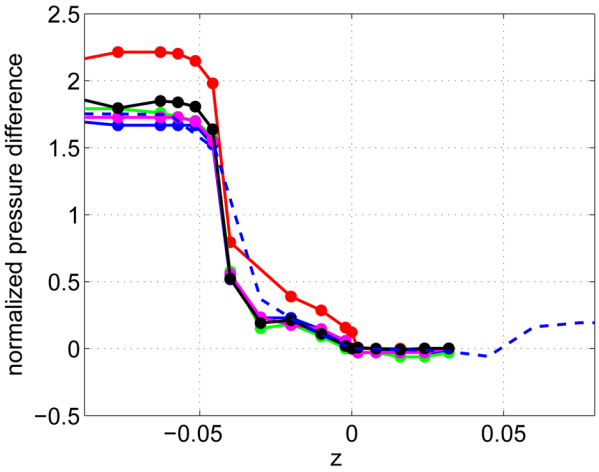

(b) normalized pressure difference along z

Figure 7.

Case Re_t = 3500: comparison between experimental data (solid lines) and numerical results (dashed line) for (a) normalized axial velocity (30) along the z axis and (b) normalized pressure difference (31) along the z axis. The legend in (a) is common to both subfigures.

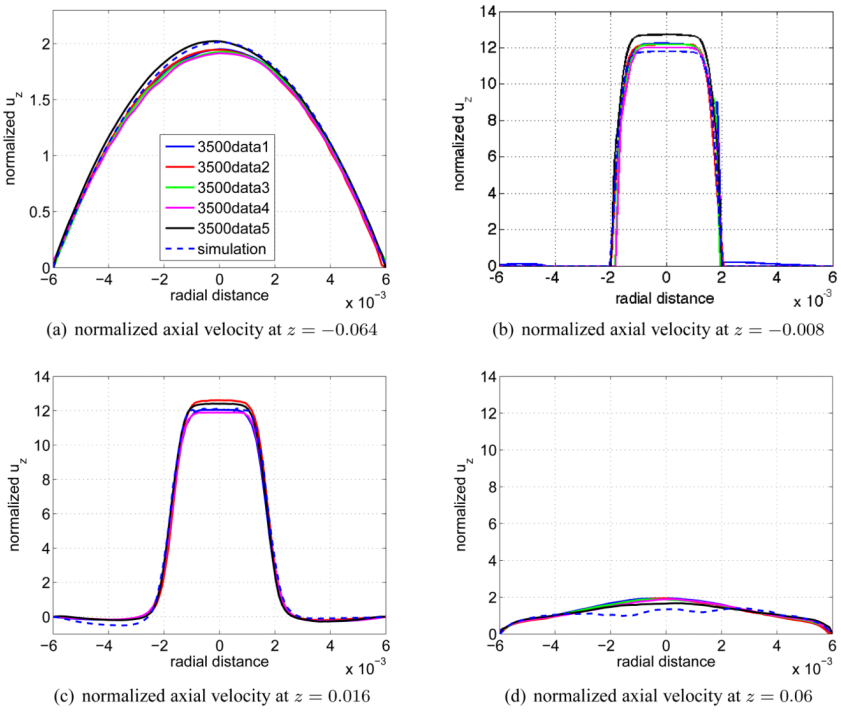

(a) normalized axial velocity at $z = -0.064$

(b) normalized axial velocity at $z = -0.008$

(c) normalized axial velocity at $z = 0.016$

(d) normalized axial velocity at $z = 0.06$

Figure 8.

Case Re_t = 3500: comparison between experimental data (solid lines) and numerical results (dashed line) for normalized axial velocity (30) at (a) $z = -0.064$, (b) $z = -0.008$, (c) $z = 0.016$, and (d) $z = 0.06$. The legend in (a) is common to all four subfigures.

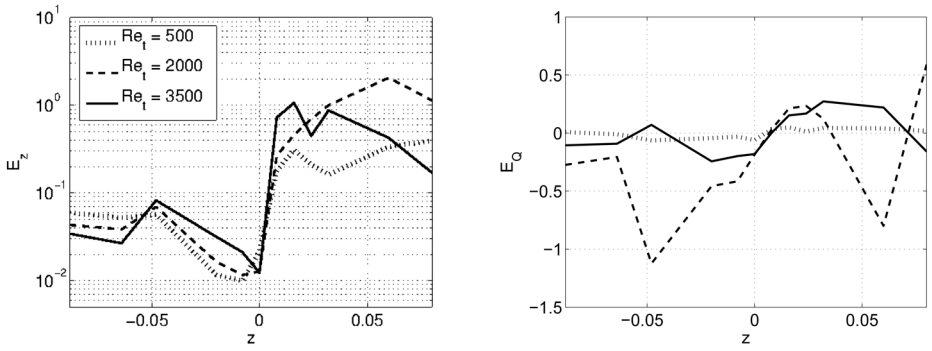

(a) Validation metric E_z (b) conservation of mass error metric

Figure 9.

(a) Validation metric E_z (32) in semi-logarithmic scale and (b) conservation of mass error metric E_Q (33) as a function of the position along the *z* axis for Re_t = 500, 2000, 3500. The legend in (a) is common to both subfigures.

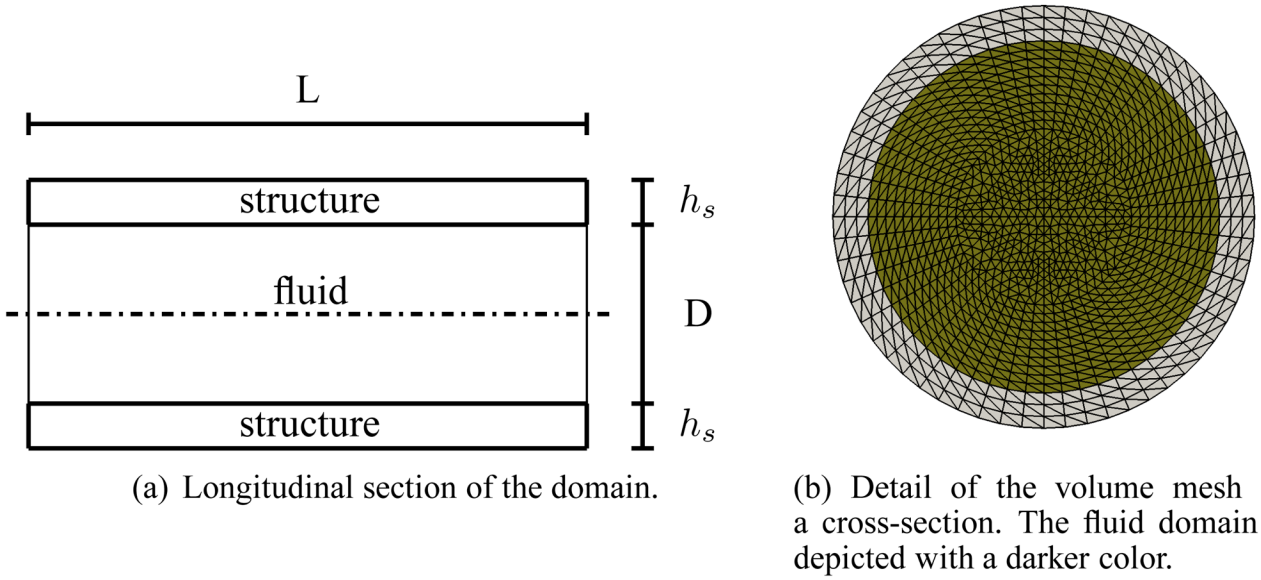

(a) Longitudinal section of the domain.

(b) Detail of the volume mesh on a cross-section. The fluid domain is depicted with a darker color.

Figure 10.
Computational domain for the FSI benchmark.

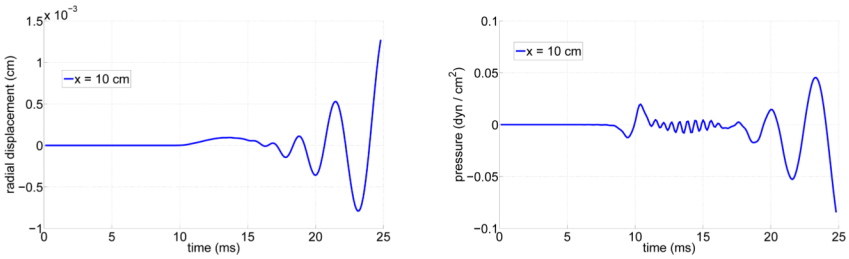

(a) Radial displacement of outer wall surface (b) Pressure along the tube centerline

Figure 11.

Time history at the outlet section (abscissa = 10 cm) of the (a) radial displacement of the outer wall and (b) fluid pressure on the tube axis. Around $t = 0.02$ s the propagating wave reaches the outlet section and wave reflections take place. Results obtained on the finest mesh were processed to generate these images.

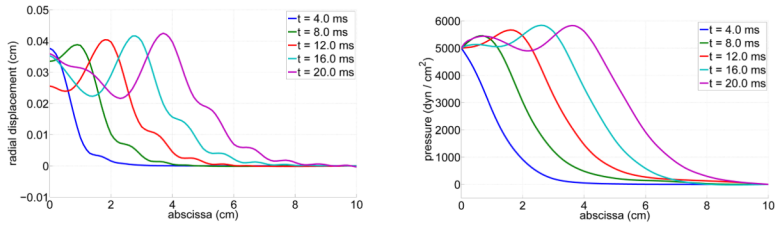

(a) Radial displacement of outer wall surface (b) Pressure along the tube centerline

Figure 12.

The wave propagation in the fluid and solid domains. Snapshots at different times of (a) the radial displacement of the outer wall surface (b) the fluid pressure along the tube centerline. Results obtained on the finest mesh were processed to generate these images.

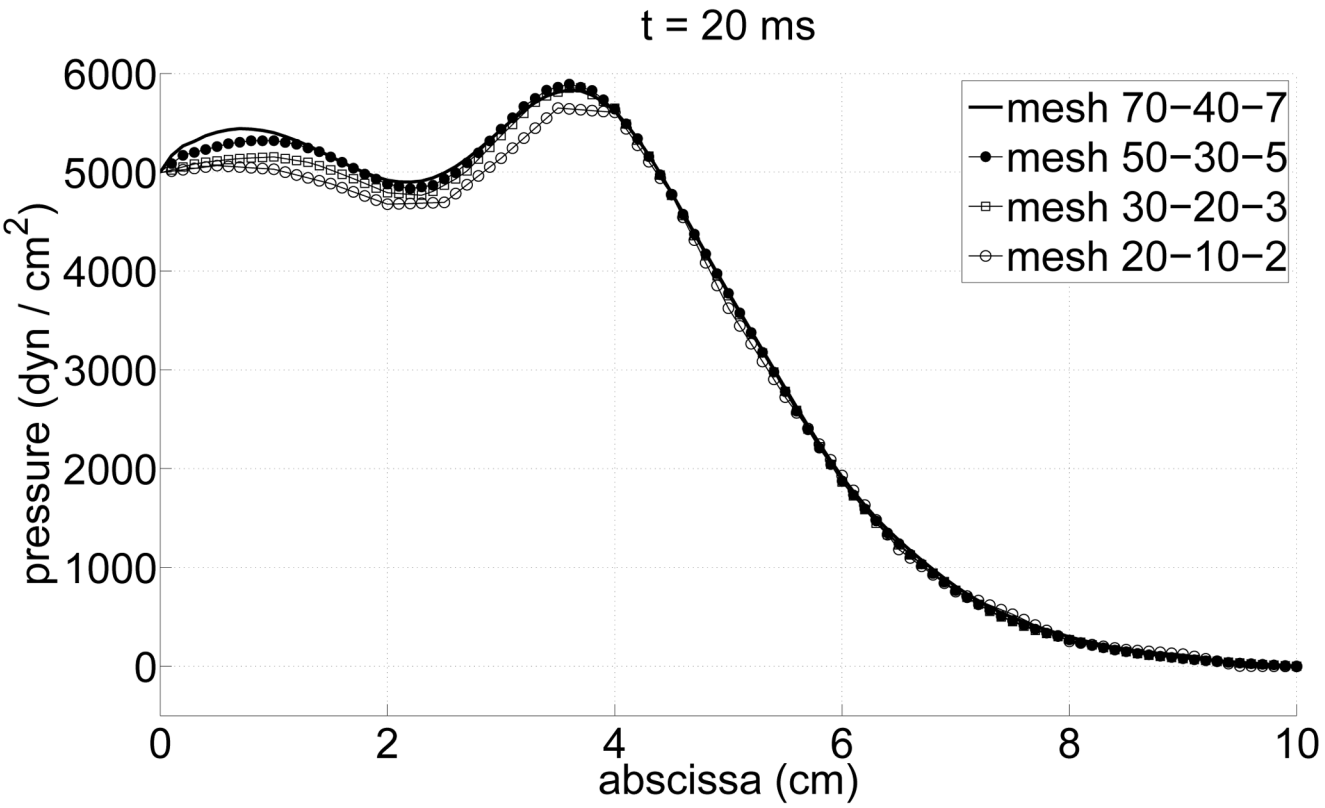

Figure 13.
The fluid pressure along the tube centerline at t = 20 ms, as computed using the four different meshes. The small discrepancies in the computed values show that substantial mesh independence is achieved using the two finest meshes.

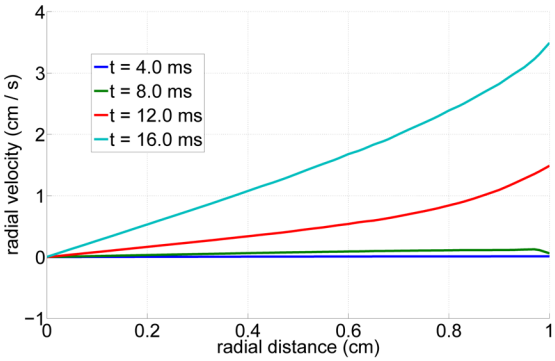

(a) Radial velocity on a cross-section at $x = 5$cm

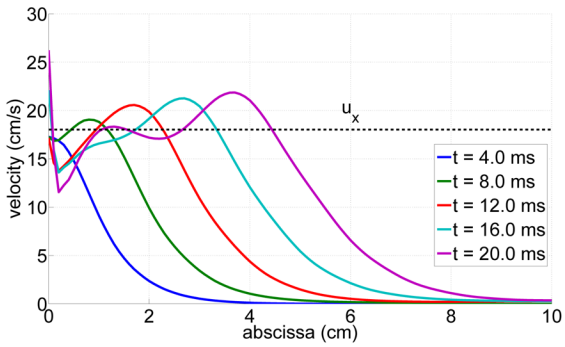

(b) Axial velocity, compared with the Joukowsky velocity u_x

Figure 14.
The simulated wave propagation phenomenon matches closely theoretical predictions. Consistently with our assumptions on the model, the radial velocity of the fluid is a linear function of the radial position apart from a thin layer near the tube wall. The fluid velocity on the axis of the pipe approximates the value predicted by Joukowsky's equation. Results obtained on the finest mesh were processed to generate these images.

Table I

Throat Reynolds number Re_t, inlet Reynolds number Re_i, and flow rate for the flow regimes under consideration.

Re_t	Re_i	flow rate Q (m^3/s)
500	167	5.2062e-6
2000	667	2.0825e-5
3500	1167	3.6444e-5

Table II

Validation metric E_z (32) at six radial sections upstream and inside the throat. Smaller values of the metric identify a better agreement with the available data.

	z = −0.088	**z = −0.064**	**z = −0.048**	**z = −0.02**	**z = −0.008**	**z = 0**
Re = 500	0.0594	0.0522	0.0565	0.0116	0.0100	0.0217
Re = 2000	0.0433	0.0384	0.0692	0.0164	0.0116	0.0127
Re = 3500	0.0343	0.0267	0.0825	0.0316	0.0212	0.0123

Table III

Validation metric E_z (32) at six radial sections downstream of the throat

	z = 0.008	**z = 0.016**	**z = 0.024**	**z = 0.032**	**z = 0.06**	**z = 0.08**
Re = 500	0.1793	0.3103	0.2096	0.1622	0.3364	0.3941
Re = 2000	0.2662	0.4595	0.6959	1.0005	2.0609	1.1355
Re = 3500	0.7231	1.0648	0.4469	0.8729	0.4247	0.1698

Table IV

Predicted pressure wave speed from numerical experiments with different mesh size.

mesh	20-10-2	30-20-3	50-30-5	70-40-7
pressure wave speed (cm/s)	274.1983	275.3064	276.4382	276.6159